Electrochemistry of Illusive Barbosalite, $Fe^{2+}Fe^{3+}_2(PO_4)_2(OH)_2$: An Iron Phosphate Related to Lipscombite Structure

Prashanth Sandineni

Kartik Ghosh

Amitava Choudhury
Missouri University of Science and Technology, choudhurya@mst.edu

Recommended Citation

Electrochemistry of Illusive Barbosalite, $Fe^{2+}Fe^{3+}_2(PO_4)_2(OH)_2$: An Iron Phosphate Related to Lipscombite Structure

Prashanth Sandineni, [1,*] Kartik Ghosh,[2] and Amitava Choudhury [1,**,z]

[1]*Department of Chemistry, Missouri University of Science and Technology, Rolla, Missouri 65409, USA*
[2]*Department of Physics, Astronomy and Materials Science and Center for Applied Science and Engineering, Missouri State University, Springfield, Missouri 65897, USA*

Barbosalite, an iron hydroxy-phosphate belonging to the family of Lazulite has been synthesized using hydrothermal route and its electrochemical property is investigated for the first time with respect to Li-ion batteries. The structure, as determined from single-crystal X-ray diffraction data, built up of undulating layers of FeO_6 octahedra, consisting of trimers and PO_4 tetrahedral units. Magnetic susceptibility measurements show predominant overall anti-ferromagnetic interactions and room temperature ^{57}Fe Mössbauer spectroscopic studies confirm the mixed 3+ and 2+ oxidation states of Fe in the compound. The compound is stable up to 400°C and undergo facile electrochemical lithium insertion. Galvanostatic charge-discharge studies indicate that up to 0.7 lithium ions per formula unit can be inserted at an average voltage of 2.6 V. The barbosalite phase seems to undergo irreversible phase transition upon lithiation as evident from the powder X-ray diffraction pattern of the reduced and oxidized phases.

Iron phosphates are extensively investigated as electrode materials for Li-ion batteries since Goodenough's group discovery of $LiFePO_4$ as an inexpensive and environmentally friendly 3.5 V cathode material for Li-ion batteries.[1] Iron hydroxy phosphates, often called basic iron phosphates,[2] are interesting class of materials that have found applications in catalysis and also tested for cathodes for rechargeable lithium-ion batteries.[3–7] These basic phosphates of iron are widespread in mineral kingdom and display rich crystal chemistry.[2] By virtue of the presence of hydroxide ion in these iron phosphates, FeO_n polyhedra are either corner- or edge-/face-shared to yield finite or infinite chains of iron-centered polyhedra.[2] Amongst the various hydroxy phosphates, the presence of a face-shared trimeric unit, termed as *h*-cluster by P. B. Moore, is quite common and different connectivities between the *h*-clusters with other iron-oxo clusters and phosphate tetrahedral unit create different structure types.[2] Mineral families of basic iron phosphates that contain the octahedral face-sharing three-cluster include rockbridgeite $(FeFe_4(OH)_5(PO_4)_3)$,[2] beraunite $(Fe_3(OH)_{2.5}(PO_4)_2(H_2O)_3)$,[8] lipscombite $(Fe^{2+}Fe^{3+}_2(PO_4)_2(OH)_2)$[9,10] and barbosalite $(Fe^{2+}Fe^{3+}_2(PO_4)_2(OH)_2)$[11] etc and all of them seem to have mixed valency of iron. In lipscombite, the face-shared trimeric units are further face-shared to form the infinite face-shared chain of octahedra where Fe is partially occupied with $\frac{3}{4}$ Fe/octahedra in 1:2 ratio of Fe^{2+} and Fe^{3+} in the chain. Barbosalite, a member of Lazulite family, is related to lipscombite in which instead of disordered face-shared chain, iron octahedra are ordered and they form isolated trimer of *h*-cluster. The ferric end members $(Fe_{2-y}\square_y(PO_4)(OH)_{3-3y}(H_2O)_{3y-2}$ ($y = 2/3$ or 0.82)] of the lipscombite structure type with tetragonal symmetry has been extensively studied as cathode for Li-ion batteries.[6,12–20] Apart from this, hydroxy Tavorite has been studied in recent years as cathodes for Li-ion batteries.[7,21–24] Tavorite, unlike lipscombite, has an infinite chains of corner-shared Fe-octahedra. This iron Tavorite structure-type has been a hallmark of voltage tuning through substitution of OH by more electronegative F.[21,23] Surprisingly besides these two hydroxy phosphates, no other basic iron phosphate has been investigated for lithium or sodium ion batteries.

Barbosalite with ordered Fe-sites can be considered a relative of lipscombite with every fourth octahedral site of which being empty. Therefore, intuitively it should show similar electrochemical activities as the ferric end member of lipscombite but with reduced capacity due

to $1/3^{rd}$ of Fe in +2 oxidation state. However, most of the studies reported on barbosalite are on naturally occurring minerals, there is just one report of synthetic barbosalite which involves a two-step process with two different precursors of iron.[25] In this article we report one-step syntheses of pure barbosalite and study their electrochemistry for the first time with respect to Li-ion insertion. Our synthetic barbosalite has little variation in composition with slightly increased amount of Fe^{2+} due to the dehydroxylation-hydration reaction. The synthetic barbosalite has been characterized by Mössbauer spectroscopy, magnetic measurements, IR and thermogravimetric analysis.

Experimental

Materials.—All the chemicals used in the syntheses were as-purchased and without further purification. $FeSO_4·7H_2O$, H_3PO_4 (85%), and H_3BO_3 (Reagent grade) were purchased from Fischer Scientific. $LiOH·H_2O$ and NaF (99%, Reagent grade) were purchased from Alfa Aesar and Aldrich, respectively.

Synthesis.—We have employed two different one-step hydrothermal syntheses routes to prepare phase pure barbosalite. In the first approach the compound was synthesized from a mixture of 0.278 g of $FeSO_4·7H_2O$ (1 mmol), 0.062 g of H_3BO_3 (1 mmol), 0.042 g of NaF (1 mmol) and 0.13 ml of H_3PO_4 (2 mmol) in 5 ml of H_2O in a 23 ml capacity Teflon-lined stainless steel Paar acid digestion bomb. The reactants were first dissolved in 5 ml of water with constant stirring in a Teflon beaker covered with a lid, which was then placed in the steel autoclave, sealed tightly, and placed in a 185°C pre-heated oven. The autoclave was heated for 24 hours, followed by cooling down to room temperature in ambient air. The product of the reaction consisted of dark colored crystals, which was then filtered and washed with hot water (yield 72%). Since both sodium and fluorine were absent (from EDS analysis) in the final composition, we explored the synthesis with NaOH instead of NaF but it led to a different phase (see Table S1). Subsequently we used LiOH and was able to produce pure phase of barbosalite. In this second approach, hydrothermal reaction was carried out at 175°C for 3 days by taking a mixture of 1.39 g of $FeSO_4·7H_2O$ (5 mmol), 1 ml of H_3PO_4 (10 mmol), 0.31 g of H_3BO_3 (5 mmol), and 0.21 g of $LiOH·H_2O$ (5 mmol) in 9 ml H_2O in a 23 ml capacity vessel. The dark color product (yield 75%) was isolated following similar work up approach as above. It is to be noted here that in both approaches, presence of H_3BO_3 was essential to produce barbosalite. Both the methods produce crystals amenable for single-crystal X-ray diffraction study. Various trials of syntheses are given in Table S1 (S.I.).

*Electrochemical Society Student Member.
**Electrochemical Society Member.
zE-mail: choudhurya@mst.edu

Table I. Crystal data and structure refinement for $Fe_3(PO_4)_2(OH)_2$ from NaF route.

Empirical formula	$Fe_3(PO_4)_2(OH)_2$
Formula weight	391.51
Temperature	298(2) K
Wavelength	0.71073 Å
Crystal system	Monoclinic
Space group	$P\,2_1/c$
a/Å	7.309(4)
b/Å	7.479(4)
c/Å	7.497(5)
β/°	119.836(6)
Volume	355.5(4) Å^3
Z	2
Density (calculated)	3.657 g/cm^3
Absorption coefficient	6.535 mm^{-1}
F(000)	380
Goodness-of-fit on F^2	1.044
Final R indexes [I>2sigma(I)]	R1 = 0.0487, wR2 = 0.1284
R indexes (all data)	R1 = 0.0574, wR2 = 0.1365

Table III. Selected bond lengths [Å] and Bond Valence Sum values for the compound.

Atom-Atom	d (Å)	Atom-Atom	d (Å)	Atom-Atom	d (Å)
P1 – O2	1.520(6)	Fe1 – O3[#1]	2.065(7)	Fe2 – O1[#6]	1.927(6)
P1 – O1	1.521(6)	Fe1 – O3[#2]	2.065(7)	Fe2 – O2	1.929(6)
P1 – O3	1.536(6)	Fe1 – O5[#3]	2.116(5)	Fe2 – O5	2.018(5)
P1 – O4	1.543(6)	Fe1 – O5[#4]	2.116(5)	Fe2 – O4[#7]	2.048(6)
		Fe1 – O4[#5]	2.138(5)	Fe2 – O3[#8]	2.071(6)
		Fe1 – O4	2.138(5)	Fe2 – O5[#1]	2.122(5)
BVS, P1 = 5.062		BVS, Fe1 = 1.846		BVS, Fe2 = 3.025	

Symmetry transformations used to generate equivalent atoms:
[#1] x, -y+1/2, z-1/2.
[#2] -x, y-1/2, -z+1/2.
[#3] -x+1, -y, -z+1.
[#4] x-1, y, z-1.
[#5] -x, -y, -z.
[#6] -x+1, y-1/2, -z+1/2.
[#7] x+1, -y+1/2, z+1/2,
[#8] -x+1, -y+1, -z+1.

Chemical reduction.—The compound was subjected to chemical reduction using LiAlH$_4$. 0.1842 g (0.94 mmol) of the compound was mixed with 0.03567 g (0.94 mmol) of LiAlH$_4$ in Tetrahydrofuran (THF) and was stirred continuously at room temperature in an argon filled glove box for 3 days and then the reaction mixture was filtered, washed with THF and dried under vacuum without exposing to air.

Material characterization

Single-crystal X-ray diffraction.—Single-crystal X-ray diffraction data were collected from crystals obtained from both the syntheses. The intensity data sets were collected on Bruker Smart Apex diffractometer with monochromated Mo K$_\alpha$ radiation (0.7107 Å). The data sets were collected at room temperature using SMART[26] software employing a scan of 0.3° in ω with an exposure time of 20 s per frame. The cell refinement and data reduction were carried out with SAINT[27] and the program SADABS[27] was used for the absorption correction. The structures were solved by direct methods using SHELX-97 and difference Fourier syntheses.[28] Full-matrix least-squares refinement against |F^2| was carried out using the SHELXTL-PLUS suite of programs.[27] The compound crystallizes in monoclinic crystal system and solved in $P2_1/n$ space group. However, before the final refinement the space group was transformed from $P2_1/n$ to $P2_1/c$ and refined again. Crystals were twinned and a TWIN law was determined using TwinRotMat routine in PLATON[29] and utilized in the final refinement performed with SHELXL-2014 using shelXle software.[30] The crystallographic parameters for the structure solution are given in Table I. The final atomic coordinates and selected interatomic distances are given in Tabless II and III for the structure

Table II. Atomic coordinates and equivalent isotropic displacement parameters (Å^2) of $Fe_3(PO_4)_2(OH)_2$. U(eq) is defined as one third of the trace of the orthogonalized Uij tensor.

| Atom	Wyckoff	x/a	y/b	z/c	U(eq)
P(1)	4e	0.2465(3)	0.3846(3)	0.2441(3)	0.008(1)
Fe(1)	2a	0.0000	0.0000	0.0000	0.011(1)
Fe(2)	4e	0.7319(2)	0.2320(1)	0.5069(2)	0.009(1)
O(1)	4e	0.3035(11)	0.4960(8)	0.1090(9)	0.014(1)
O(2)	4e	0.4304(9)	0.2624(8)	0.3786(9)	0.015(1)
O(3)	4e	0.1955(10)	0.5111(8)	0.3749(9)	0.014(1)
O(4)	4e	0.0500(9)	0.2679(7)	0.1142(9)	0.011(1)
O(5)	4e	0.7375(8)	0.1337(8)	0.7603(8)	0.010(1)

solution from the crystals of NaF-based synthesis, while same data for LiOH-based synthesis are supplied as supplementary materials (see Tables S2, S3, and S4 in S.I.). It is to be noted here that crystal structure solutions from both the syntheses indicate absence of alkali ions, which is supported by EDS for Na and chemical analysis for Li. The final composition derived from crystal structure solutions was $Fe_{0.5}^{2+}Fe^{3+}(PO_4)(OH)$ or $Fe_3(PO_4)_2(OH)_2$, however, Mössbauer spectroscopic data (discussed later) indicated presence of slightly excess Fe^{2+} (Fe^{3+}:Fe^{2+} = 61.8:38.2) than crystallographically derived composition. Due to the absence of any alkali ions into the structure, the only way the excess Fe^{2+} can be explained is by invoking partial replacement of hydroxyl by water through the reduction of Fe^{3+} leading to a final composition of $Fe_{1.5}(PO_4)(OH)_{0.93}(H_2O)_{0.07}$ or $Fe_3(PO_4)_2(OH)_{1.86}(H_2O)_{0.14}$.

Powder X-ray diffraction (PXRD).—The laboratory PXRD pattern was obtained from a PANalytical X'Pert Pro diffractometer equipped with a Cu K$_{\alpha1,2}$ anode and a linear array PIXcel detector over a 2θ range of 5 to 90° with an average scanning rate of 0.0472° s^{-1}. Phase purity of the samples was evaluated by laboratory PXRD through the direct comparison with the simulated pattern generated from the atomic coordinates of single-crystal XRD solution (Figure S1, supporting information). However, to confirm the validity of single-crystal structure solution and to determine absence of any impurity phase(s) we have employed high-resolution synchrotron PXRD (S-PXRD) data collected from Advanced Photon Source (APS) in Argonne National Laboratory. Rietveld refinement using GSAS-II[31] of the S-PXRD data from the NaF-based synthesis route converged very well and confirmed absence of any impurity phase(s). A plot of Rietveld refined data of S-PXRD converted into Cu Kα wavelength over a 2θ range of 2 to 90° is given in Figure 1, however the whole range of S-PXRD from 2θ = 0.5 to 50° in λ = 0.412832 Å has been provided in supporting information (Figure S2).

Mössbauer spectroscopy.—^{57}Fe Mössbauer experiment was performed in transmission geometry at room temperature using a conventional constant acceleration spectrometer. The data were collected using a ^{57}Co (25 mCi) gamma-ray source embedded in a Rh matrix. Velocity calibration and isomer shifts are given with respect to α-Fe foil at room temperature. The Mössbauer data were analyzed by Lorentzian line fitting using RECOIL software.[32]

Magnetic measurements.—The variable temperature magnetic susceptibility measurements of the compound (as-prepared) was carried out in the temperature range 5–300 K using Quantum Design
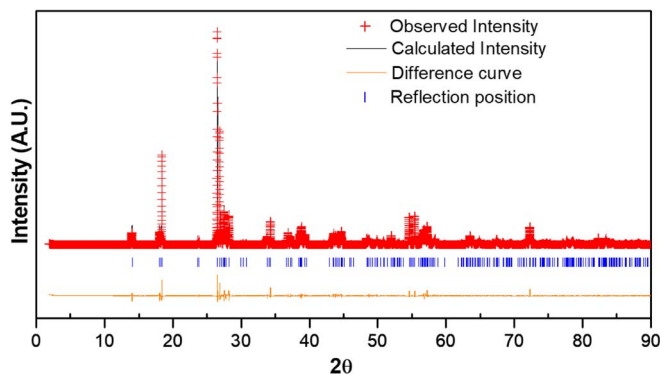
Figure 1. Rietveld refinement of synchrotron XRD data converted to standard PXRD with Cu Kα (λ = 1.540598 Å) of $Fe_3(PO_4)_2(OH)_{1.86}(H_2O)_{0.14}$ showing the observed, calculated and difference curve.

SQUID magnetometer at 1T applied field while warming up from 5–300 K while the sample was cooled under zero applied field (ZFC). Isothermal magnetization measurements were performed at 5 K between 0 to 5 T applied field.

Thermogravimetric analysis (TGA).—TGA has been performed with a TA instruments Q50 TGA from room temperature to 800°C with a scan rate of 10°C min⁻¹ under nitrogen atmosphere.

IR spectroscopy.—The IR spectrum was collected using Thermo Nicolet iS50 FT-IR spectrometer over 400–4000 cm⁻¹ on a sample using ATR mode.

SEM.—The morphology of the powder sample was studied by scanning electron microscopy (Hitachi S 4700 FESEM) at 5 kV operating voltage.

Electrochemical testing.—To evaluate the electrochemical activities of the samples, the as-synthesized compounds were subjected to ballmilling thoroughly after mixing with super P conductive carbon in a SPEX 8000 miller for 3 hours to reduce the particle size. Polyvinylidene fluoride (PVDF) was then added to the active material as the binder and an optimum amount of N-methyl-2-pyrrolidone (NMP) was added to dissolve the PVDF. The resulting slurry was further ball milled for another 20 minutes to obtain a homogeneous viscous mixture. The ratio of the active material, conducting carbon, and the binder in the cathode mix was 75: 15: 10 and 65:25:10. The slurry of cathode mix was then spread onto a flat sheet of carbon-coated aluminum current collector with the help of a glass rod, transferred into a vacuum oven and dried overnight at 85°C.

For electrochemical tests, CR2032 type coin cells were fabricated. The composite cathode film was cut into circular disks (3/8 inch diameter) with 4.0–5.0 mg of active material loading and transferred into an argon filled glove box with an oxygen concentration below 2.0 ppm. The cathode disk and Li anode (0.75 mm thickness Li ribbon cut into circular disk) were assembled in the coin cell casing with a Celgard 2325 circular sheet placed between the two electrodes as the separator. The electrolyte, 1 M solution of $LiPF_6$ in DMC–EC (1:1) was then added and the cell was sealed with a coin cell crimper. The prepared cells were aged for equilibration for about 12 hours before electrochemical testing.

Cyclic voltammograms were obtained using a PAR EG&G potentiostat/galvanostat model 273 in the potential range of 1.5–4.0 V (vs. Li/Li⁺) with a scan rate of 0.05 mV s⁻¹. Voltage composition profiles were obtained using galvanostatic charge/discharge experiments on an Arbin Instruments battery tester, model BT2043, on the same potential limits as CV at various C-rates. EIS spectra were obtained using biologic instruments SP-150 with the coin cells in the frequency range from 0.1 Hz to 1 MHz, by applying 5 mV AC amplitude.

Results and Discussion

Synthesis and structure.—Only synthesis of barbosalite reported in the literature involves a two-step lengthy process. An Fe(II)-phosphate precursor, $Fe_3(PO_4)_2 \cdot 8H_2O$ (vivianite) and an amorphous Fe(III)-phosphate precursor was digested first and then the product from the first step was again digested with additional phosphoric acid with a total duration of 10 days at 200°C.[25] On the other hand, we have used a low temperature one-step hydrothermal route for synthesis of barbosalite. Our initial aim was to partly substitute bridging hydroxide with fluoride to boost the insertion voltage similar to tavorite or kagomé lattice.[23,33] However, fluoride could not be inserted but the role of NaF was essential as a mineralizer for the barbosalite phase formation. Similarly, boric acid was also essential as a pH modulator and mineralizer which allowed maintenance of required acidic pH and high ionic strength enabling crystal growth of pure crystals. Since neither Na nor F got incorporated into the structure, we could successfully synthesize barbosalite using LiOH in place of NaF. However, there is a subtle difference in the composition of our barbosalite $(Fe_3(PO_4)_2(OH)_{1.86}(H_2O)_{0.14})$ compared to naturally occurring or previously reported synthetic barbosalite $(Fe_3(PO_4)_2(OH)_2)$. From Mössbauer study we have found slight excess of Fe(II) in our synthetic barbosalite which can be attributed to the exchange of hydroxide with water, since we have used almost 18 ml and 6.5 ml of water/g of $FeSO_4 \cdot 7H_2O$, respectively, for the NaF and LiOH-based synthesis, which is quite an excess compared previously reported synthesis (2ml of water/g of Fe-phosphate precursor). Similar dehydroxylation-hydration has been previously found in the ferric end member of lipscombite compensated by iron vacancy.[6]

The crystal structure of barbosalite has been adequately discussed in the literature. Here we will briefly discuss the structure and highlight the differences with lipscombite phase. Figure 2a shows the asymmetric unit of the compound, which contains seven non-hydrogen atoms, 2 Fe, 1 P, and 5 O. Out of two Fe, one is located in a special position, on the center of inversion (2a, Wyckoff site), while rest of the atoms are in general position, (4a, Wyckoff site). Out of 5 oxygen atoms, four belong to the phosphate moiety and the 5th oxygen is part of a mixed hydroxide/water. All the Fe atoms are in octahedral coordination with some degree of distortion with Fe – O distances in the range 1.926(5) – 2.157(5) and 2.056(5) – 2.109(4) Å, respectively, for Fe1 and Fe2. Figure 3 shows the packing diagram where the structure can be described as consisting of undulating layers of FeO_6 octahedra formed by the trimers of Fe1-Fe2-Fe1-centered face-shared octahedra (Figure 2b) connected through Fe-O-Fe linkages. Each trimer is connected to 4 different trimers through corner sharing at the hydroxide (O5-H) oxygen. Such layers are cross linked through corner sharing of PO_4 tetrahedra yielding a three dimensional framework of octahedra and tetrahedra with a narrow 4-membered ring channel along *c*-axis. This channel is a consequence of ordering of Fe sites in barbosalite with one Fe in +2 and the other in +3 oxidation state, unlike lipscombite where that empty site is occupied by another Fe but with two Fe sites having partial occupancy. As a result instead of an isolated trimer of face-shared octahedra, lipscombite contain infinite chains of face-shared octahedra of Fe^{2+} and Fe^{3+} which are crosslinked by both FeO_6 octahedra and PO_4 tetrahedra. In the ferric end member of lipscombite there is only one crystallographically distinct Fe site with partial occupancy resulting in infinite face-shared octahedral chain with high concentration of Fe vacancy. Besides the narrow channel along the *c*-axis, barbosalite has another four-membered ring channel when viewed along [−2, −2, 1] direction, this channel is a common feature in barbosalite and lipscombite as can be seen along [1 1 0] direction and *a*-axis for mixed valent and ferric lipscombite, respectively (Figure 4). This remarkable similarity has also been reflected in the PXRD patterns of these compounds as shown in Figure 4. When viewed along the [0 1 0] direction, we can clearly see the ordering of trimers which is not clearly visible from [−2, −2, 1] direction (Figure S3, S.I.).

Spectroscopic and thermogravimetric analysis.—FT-IR spectroscopy has been used (Figure S4, S.I.) to further characterize the
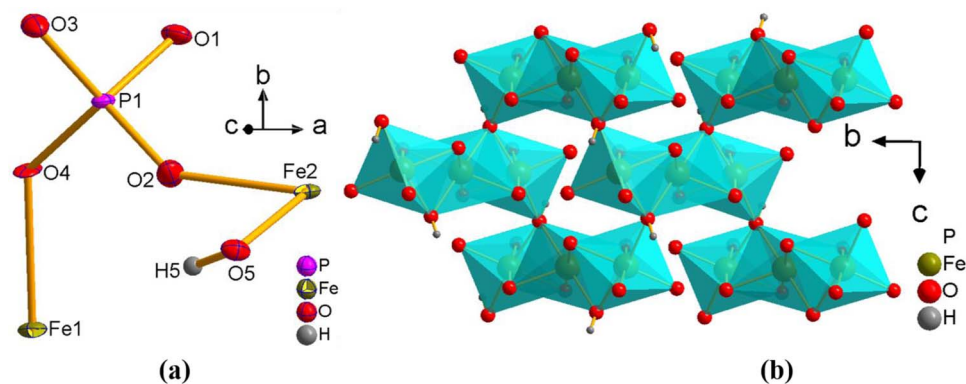
Figure 2. Asymmetric unit (a) and the interconnectivity of the trimers of Fe1-Fe2-Fe1 along *a*-axis (b) of the compound, $(Fe_3(PO_4)_2(OH)_{1.86}(H_2O)_{0.14})$.

chemical nature of the inter-atomic bonding in the as-prepared sample. The IR spectra of the compounds from the two syntheses routes show prominent bands at 3300 cm^{-1} region which can be attributed to the O – H stretching mode and band at 1585 cm^{-1} to O – H bending modes from the bridging H_2O. The peaks at 900–1100 can be attributed to the symmetric and antisymmetric stretching modes of P – O in phosphate group. The symmetric and antisymmetric bending modes of P – O can be seen from 400–600 cm^{-1}.

TGA has been performed to determine the thermal stability of the compounds (Figure 5). The TGA curves indicate that the compound is stable up to 400°C irrespective of synthetic routes and after that it starts to lose weight till 650°C which can be attributed to the loss of one H_2O molecule based on the observed weight loss of 4.1% (theoretical = 4.6%) to form Fe_2OPO_4 and $FePO_4$ as determined from the PXRD of heated residue. (Figure S5, S.I.).
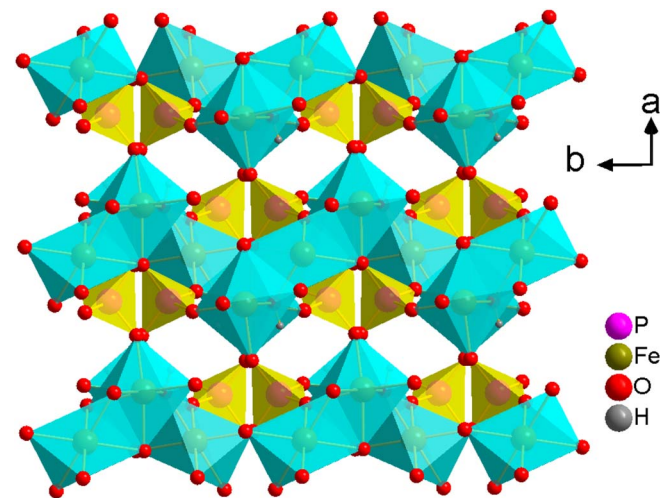
Figure 3. Perspective view of the structure of $Fe_3(PO_4)_2(OH)_{1.86}(H_2O)_{0.14}$ showing packing diagram along *c*-axis.

SEM analysis.—To evaluate the particle size, hand-ground (using mortar pestle) material was used for the SEM analysis (Figure S6, S.I.). The average particle size of the compound ranged from 3–20 μm in the hand-ground sample.

Mössbauer spectroscopy.—Figure 6 shows the Mössbauer spectra for the compounds synthesized by two different routes. Isomer shift (IS) and quadrupole splitting (QS) parameters derived from the Lorentzian fittings of the peaks are listed in Table IV. Well-ground powder of as-prepared samples were used for measurements. IS and QS values are in well accordance with the Fe^{+3} and Fe^{2+} sites of barbosalite reported by Redhammer et al.[34] However, our samples yielded slightly higher percentage of Fe^{2+} population, which is stabilized by the exchange of hydroxide with water. The IS and QS values also correlate with the high spin Fe^{2+} and Fe^{3+} ions in octahedral coordination.[35]

Magnetic properties.—The temperature dependent ZFC magnetic susceptibility $\chi_M(T)$, the corresponding inverse molar susceptibility $\chi_M^{-1}(T)$ and isothermal field dependent magnetization $M(H)$ for the as-synthesized compound (NaF route) is given in Figure 7. The onset of magnetic ordering can be seen at 169 K with a jump in magnetic susceptibility as shown in Figure 7 at an applied field of 1 T. This jump resembles more like a ferromagnetic transition but the linear fitting of the inverse susceptibility above 250 K yields a high negative Θ_p value (−332 K) indicating predominant antiferromagnetic interactions. Magnetic moment/Fe (6.63 μ_B) as calculated from the curie constant, C, derived from the linear fit yields a higher value than theoretically expected for a 62% Fe^{3+} and 38% Fe^{2+} iron site. This may be due to the fact that the temperature region between 250–300 K does not reside on a paramagnetic region and one has to go above the room temperature to be in the purely paramagnetic region. The overall interactions can be described as antiferromagnetic with a ferromagnetic component due to competing anti-ferromagnetic and ferromagnetic interactions between the Fe^{3+} centers (inter-trimer) and Fe^{2+} and Fe^{3+} (within the trimer). The saturation magnetization at 5 K is about 0.12 Nβ, which is quite less than the theoretical saturation magnetization ($Ms = gS$ Nβ) of fully ordered magnetic moment of either four (high spin Fe^{2+}) or five (high spin Fe^{3+}) unpaired electrons

Table IV. The fitted ^{57}Fe Mössbauer spectroscopic values for Isomer Shift (IS) and Quadrupole Splitting (QS) of the as-synthesized compounds.

| NaF route	Sites	IS(δ) (mm.s^{-1})	QS (ΔE_Q) (mm.s^{-1})	Site population (%)
Fe^{3+}	Doublet site-1	0.433(3)	0.449(5)	61.8
Fe^{2+}	Doublet site-2	1.087(3)	3.533(3)	38.2
LiOH route	Sites	IS(δ) (mm.s^{-1})	QS (ΔE_Q) (mm.s^{-1})	Site population (%)
Fe^{3+}	Doublet site-1	0.429(3)	0.435(5)	62.4
Fe^{2+}	Doublet site-2	1.087(3)	3.506(3)	37.6
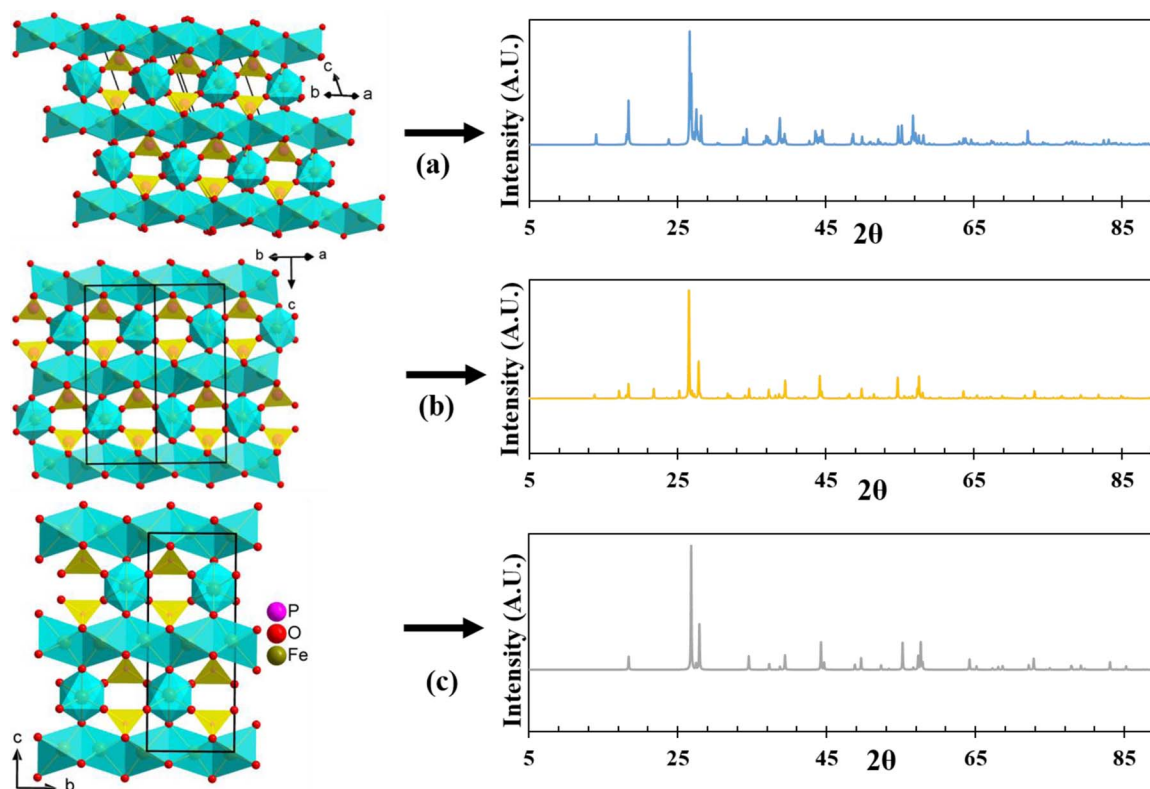
Figure 4. Comparison of 3D structures of barbosalite (a), lipscombite (b), and ferric lipscombite (c) with their simulated PXRD patterns.

(inset of Figure 7). More interestingly the magnetization curve remains negative up to an applied field of 1000 Oe, after which it becomes positive. The negative magnetization in barbosalite has been observed previously,[34] however, actual cause of negative magnetization needs further investigation.

Electrochemistry

Cyclic voltammetry.—Cyclic voltammetry tests were conducted on the fabricated Li-ion coin cells to get an idea of the Li-insertion (cathodic reduction) and Li-extractions (anodic oxidation) voltages. Figure 8 shows the first three cycles of cyclic voltammograms, when the cell was subjected to a voltage scanning between 1.5–4.0 V. Open circuit voltage (OCV) was at 2.99 V. The battery was discharged first yielding an onset of reductive lithiation at 2.55 V with a peak at 2.45 V and the corresponding oxidation peak was at 2.75 V. The potential at the reduction peak increased in the subsequent cycle to 2.5 V and at

same time oxidation peak decreased to 2.7 V, with an onset of oxidation at 2.3 volt. From the oxidation and reduction peaks, the average voltage can be estimated to be around 2.6 V. It is also to be noted here that
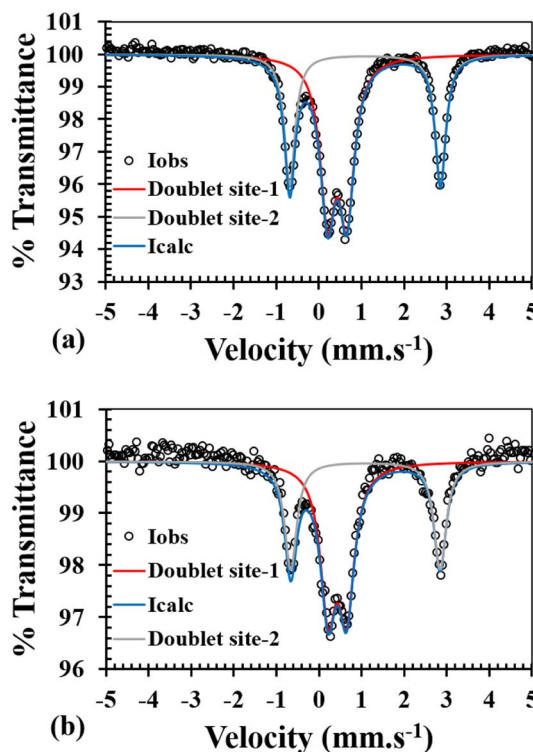
**Figure 6.** Mössbauer spectra of the compounds prepared from NaF route (a) and LiOH route (b).
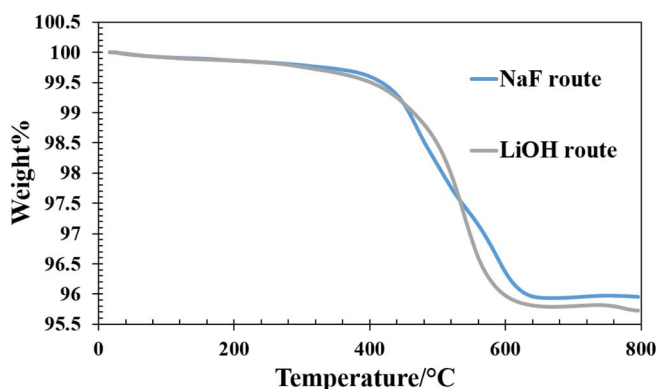
**Figure 5.** TGA curves of the compound $Fe_3(PO_4)_2(OH)_{1.86}(H_2O)_{0.14}$ from NaF and LiOH routes.
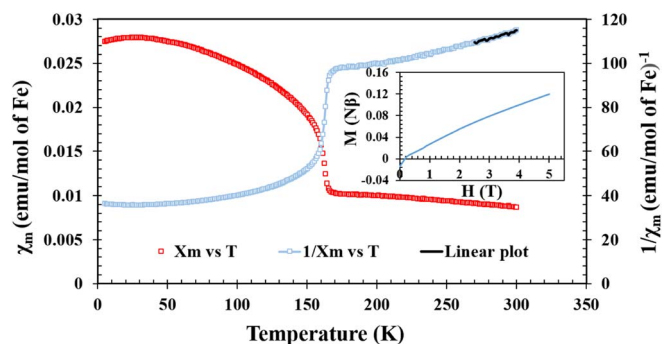
Figure 7. Temperature dependence of molar magnetic susceptibility (χ_m) and inverse molar magnetic susceptibility (χ_m^{-1}) of $Fe_3(PO_4)_2(OH)_{1.86}(H_2O)_{0.14}$ synthesized by NaF route. (Inset shows M vs H plot).

during reduction it exhibit strong cathodic current with a sharp peak while during the anodic oxidation it shows a broad peak spanning between 2.3 to 3.5 volt.

Galvanostatic charge-discharge.—The galvanostatic charge-discharge experiments were done at various slow C-rates and the cutoff potentials were set in the range 1.5–4.0 V for all the tests (Figure 9). Assuming a complete one electron process per Fe atom, the theoretical capacity of the compound can be calculated to be 136.90 mAh.g^{-1}. Figure 9 shows the charge-discharge profiles at C/50. The first discharge delivered a capacity of 47 mAh.g^{-1}, which on subsequent cycles increased to 55 mAh.g^{-1}. Subsequently at various comparatively faster C-rates specifically, at C/20, C/10 and C/5, a very stable capacity of 52, 50 and 46 mAh.g^{-1}, respectively, was achieved (Figure 10). The decrease in capacity with the increasing C-rate was minimum. After several cycles of faster C-rates when we returned to slower C-rate (C/50), the capacity further increased to 69 mAh.g^{-1}, which is equivalent to insertion of 0.5 lithium (Figure 10). To further increase the capacity, we increased the percentage of carbon in the cathode composite from 15% to 25% assuming electronic conductivity could be a factor impeding achievement of full theoretical capacity. Similar charge-discharge tests on the higher carbon percentage in the cathode mix resulted in substantial enhancement in the achievable capacity (Figures 9 and 10). In the respective C-rates starting from C/50 and going through C/20, C/10, C/5 and again returning to C/50 in the 20th cycle we observed an increase of 10 −15 mAh.g^{-1} capacity. More interestingly when the cell was further cycled for another 20 cycles in similarly varying C-rates the capacity further jumped to 95 mAh.g^{-1} in the 40th cycle in C/50 rate. Even in C/5 rate a capacity of 65 mAh.g^{-1} can be achieved, which was the best performance in C/50 rate with
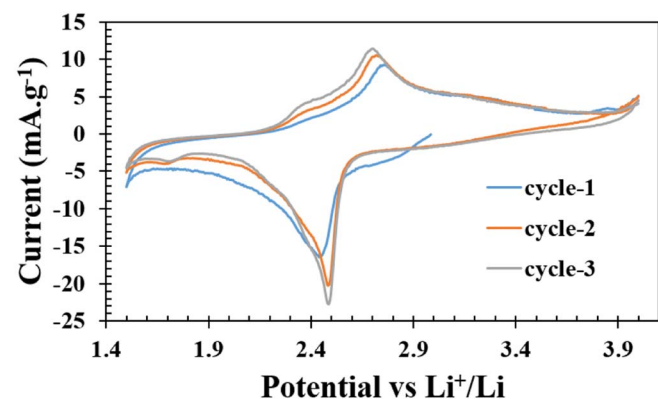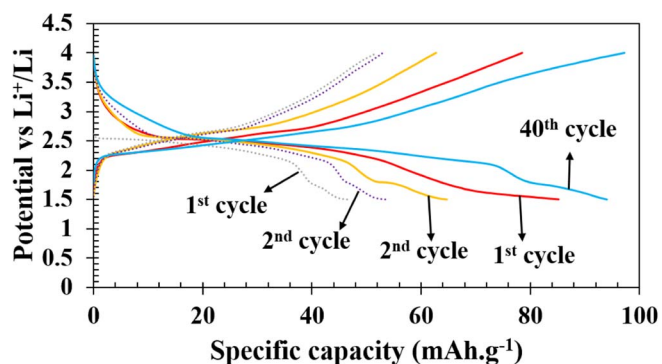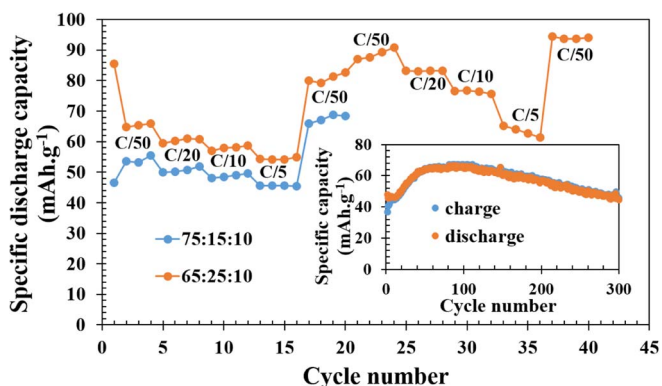

Figure 9. Galvanostatic charge-discharge profiles for Li-ion batteries at C/50 with 75:15:10 composition (shown with dotted lines, 1st and 2nd cycles) and 65:25:10 (shown with continuous lines, 1st, 2nd, and 40th cycles).

15% carbon content (Figures 9 and 10). The final achievable capacity of 95 mAh.g^{-1} is equivalent to 70% of the theoretical capacity. The cell was tested for cycle-life for 300 cycles at C/5 rate, where it continued to show capacity increase till 150 cycles and then stabilize to the initial capacity of C/5 rate (inset of Figure 10). The increase in the capacity during successive charge-discharge cycles is quite intriguing and might be associated with particle size reduction occurring during cycling or creation of conducting pathways with successive cycling or increased exposure of active materials in the electrolyte. The capacity can also increase on successive cycling due to structural transformation from a poorly electrochemically active phase to a phase with facile electrochemical activity. Another possibility could be that the active materials had some Na-substitution to begin with in the as-synthesized phase, which on successive cycling slowly got exchanged with Li and capacity increased due to decrease of equivalent weight of active material. We, therefore, also charged the battery first, which didn't yield any capacity eliminating the possibility of having Na-ion into the as-synthesized compound as was also supported by our EDS analysis (absence of Na). To better understand the capacity increase phenomena we carried out several tests with the cells that were tested for cycle-life.

Post Analysis of Cycled-Cells

Cyclic voltammetry.—We collected cyclic voltammograms for the coin cells after 100 cycles and 300 cycles from two different cells, which displayed remarkably different shape from the initial (fresh) cells (Figure S7, S.I.). The noticeable features of the cycled cells include change in the oxidation (2.5 V) and reduction (2.3 V) peaks with a decrease from the initial values of 2.8 and 2.5 V, respectively,

Figure 8. First three cycles of cyclic voltammogram of Li-ion cell made with $Fe_3(PO_4)_2(OH)_{1.86}(H_2O)_{0.14}$ as cathode and pure Li as anode.

Figure 10. Cycle index showing capacity retention at different C-rates with 75:15:10 composition (20 cycles) and 65:25:10 composition (40 cycles). (Inset shows capacity retention for 300 cycles at C/5).
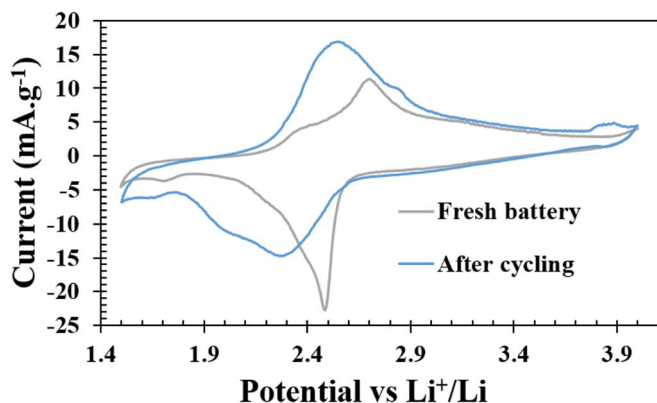
Figure 11. Comparison of cyclic voltammograms for the batteries, freshly fabricated and after cycling. (Second cycle).

along with a development of a very symmetric CV with broad rounded oxidation and reduction peaks. The area under the anodic oxidation and cathodic reduction are almost equal indicating equal kinetics of oxidation and reduction and facile electrochemistry with less polarization. More importantly lithium insertion and extraction potentials are a function of structure type and a substantial shift in their values (See Figure 11) may indicate a structural rearrangement.

Electro-impedance study.—In order to understand the kinetics of processes inside the battery, we performed electro-impedance studies on a freshly fabricated and cycled (100, 300 cycles) cells (Figure 12, fitted parameters are supplied in Table S5, S.I.). The freshly fabricated cell was fitted with one R/C element at mid frequency to high frequency region with one semicircle corresponding to the charge transfer resistance, with a low frequency tail fitted with Warburg impedance corresponding to Li-ion diffusion inside the cathode material. For the cycled cells, based on the two partially overlapped semicircle we used an extra R/C element at high frequency corresponding to SEI resistance
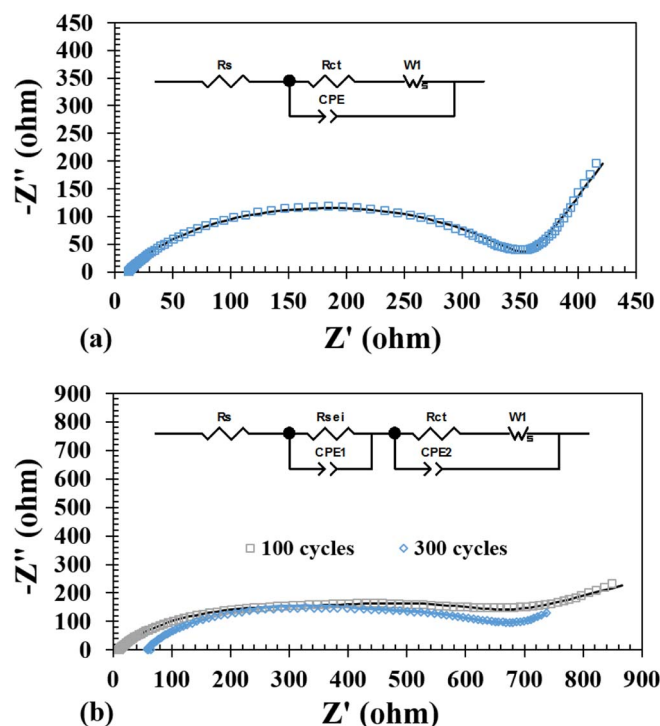
Figure 12. Nyquist plot of freshly fabricated (a) and cycled Li-ion cells (b).

(R_{SEI}), and the other semicircle for charge transfer (R_{ct}) following previous well-document work.[36,37] During cycling, the cell is expected to develop SEI (solid electrolyte interface) and thereby the combined resistance increased ($R_{SEI} + R_{ct}$). However, if we consider R_{ct} alone in all three cells, it decreases with cycling from 342 (fresh battery) to 202 ohm after 100 cycles, and showing further reduced value of 112 ohm after 300 cycles, which explains that the kinetics of the Li$^+$ charge transfer becoming facile on cycling. Such values of R_{ct} has been observed previously in phosphate-based cathode in Li-ion batteries.[38] From this observation it can be concluded that the charge-transfer in the electrolyte-electrode interface especially at cathode may be related to the transformation of the cathode materials to a more electrochemically facile phase as supported by the CV and PXRD of the cycled cell (discussed below). During cycling R_{SEI} has increased from 421 (100 cycles) to 484 ohm (300 cycles), which may be affecting capacity retention after 200 cycles.

Ex-situ pxrd characterization of discharged and charged cells.—To further understand the mechanism of the charge-discharge profiles and to evaluate if there is any structural phase transition, the ex-situ PXRDs of the charged and discharged cells were carried out. For this, the coin cells were cracked-opened inside the argon filled glove box and the cathode material in the charged and discharge state of the cells were recovered, washed with the acetone, and dried. The cathode material was then placed in an air tight cell holder, and PXRD was collected. The PXRD of the discharged phase indicates that due to successive charge-discharge process there may be structural rearrangement as evident by the emergence of a new line at $2\Theta = 25.8°$ and the new line is retained even in the charged state, supporting that the structural rearrangement is irreversible. The overall PXRDs look mostly similar to the as synthesized sample, except the development of a new peak at $2\Theta = 25.8°$. To validate the hypothesis that the structural transformation is due to lithium insertion, we carried out chemical reductive lithiation with $LiAlH_4$ by stirring the as-synthesized sample in THF with 1:1 ratio of barbosalite and $LiAlH_4$ inside Ar-filled glove box. The PXRD (Figure S8, S.I.) of the chemically reduced phase bear remarkable similarity with the electrochemically reduced/oxidized phase, corroborating well with the hypothesis that lithium insertion is causing a structural phase transition. It is to be noted here that similar phase transition has been observed recently in a vanadium oxy-phosphate, $V_4O_3(PO_4)_3$, which also belongs to lipscombite-lazulite family of structures.[39]

Possible li-sites in the structure.—It is worth discussing here the possible sites for Li-ion intercalation in barbosalite. Since the Fe-sites are ordered with an empty site at every fourth position (Wyckoff, 2*d*) of an infinite hypothetical face-shared chain of octahedra, the volume of which is appropriate for the accommodation of a lithium ion. Besides the 2*d* site there is another empty site, namely 2*b* Wyckoff site, similar to 8*c* empty channel site of the ferric end member of the lipscombite. This 8*c* site has been theoretically predicted to be the site for Li-intercalation in lipscombite.[20] Some authors also hypothesized that Li can also occupy the iron vacancy sites along with the empty channel sites in lipscombite.[19] Intuitively it is possible for Li to go either in the 2*b* empty channel site or the empty metal site, 2*d* in barbosalite, as shown in Figure 13. However, unoptimized structure with two inserted lithium ions do not produce the new line that we have observed in electrochemically/chemically reduced phase. Therefore, it can be concluded that a structural re-arrangement may be happening which may include movement of Fe-atoms in the face-shared chain. Obviously more sophisticated experiments for example, high resolution synchrotron PXRD data of the reduced Li-intercalated phase will be required to understand the structural rearrangement and locate the exact position of the Li-ion which is beyond the scope of this manuscript.
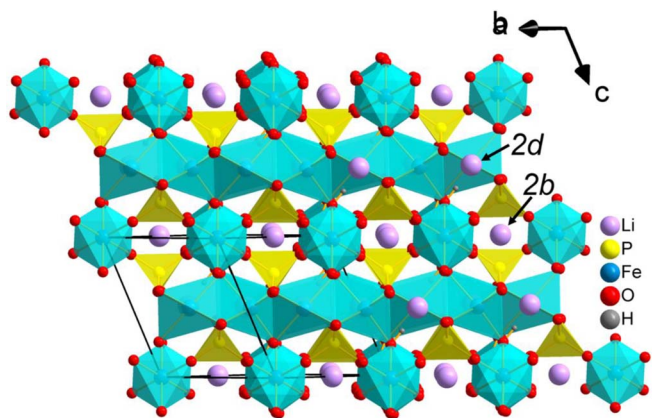
Figure 13. Perspective view of the structure of $Fe_3(PO_4)_2(OH)_{1.86}(H_2O)_{0.14}$ showing possible Li sites.

Conclusions

In this article, we have reported the synthesis of barbosalite through low-temperature hydrothermal routes. The compound has shown good achievable capacities for the Li-ion batteries with 0.7 Li insertion at an average voltage of 2.6 V. Charge-discharge profile, CV and PXRD of the cycled cell indicate structural re-arrangement due to lithium insertion. Though due to the lower capacity and smaller insertion voltage, it will not be competitive for Li-ion battery cathode but from fundamental solid state electrochemistry perspective it is an important system which complements the electrochemistry of the lipscombite structure type and reminds us about the fact that subtle difference in structure from well-studied lipscombite can have substantial impact on electrochemistry.

ORCID

Prashanth Sandineni (ID) https://orcid.org/0000-0002-2935-0261
Amitava Choudhury (ID) https://orcid.org/0000-0001-5496-7346

References

1. A. K. Padhi, K. S. Nanjundaswamy, and J. B. Goodenough, "Phospho-olivines as positive-electrode materials for rechargeable lithium batteries," *J. Electrochem. Soc.*, **144**(4), 1188 (1997).
2. P. B. Moore, "Crystal chemistry of the basic iron phosphates," *Am. Mineral.*, **55**(1–2), 135 (1970).
3. J. M. M. Millet, D. Rouzies, and J. C. Vedrine, "Isobutyric acid oxidative dehydrogenation over iron hydroxyphosphates. II. Tentative description of the catalytic sites based on Mössbauer spectroscopic study," *Appl. Catal., A.*, **124**, 205 (1995).
4. D. Rouzies, J. M. M. Millet, D. Siew Hew Sam, and J. C. Védrine, "Isobutyric acid oxidative dehydrogenation over iron hydroxyphosphates. I. Catalytic properties and role of water," *Appl. Catal., A.*, **124**(2), 189 (1995).
5. J.-M. M. Millet, "FePO catalysts for the selective oxidative dehydrogenation of isobutyric acid into methacrylic acid," *Catal. Rev. – Sci. Eng.*, **40**(1–2), 1 (1998).
6. Y. Song, P. Y. Zavalij, N. A. Chernova, and M. S. Whittingham, "Synthesis, Crystal Structure, and Electrochemical and Magnetic Study of New Iron (III) Hydroxyl-Phosphates, Isostructural with Lipscombite," *Chem. Mater.*, **17**(5), 1139 (2005).
7. N. Marx, L. Croguennec, D. Carlier, A. Wattiaux, F. L. Cras, E. Suard, and C. Delmas, "The structure of tavorite LiFePO$_4$(OH) from diffraction and GGA + U studies and its preliminary electrochemical characterization," *Dalton Trans.*, **39**(21), 5108 (2010).
8. P. B. Moore and A. R. Kampf, "Beraunite: Refinement, comparative crystal chemistry, and selected bond valences, Z. *Kristallogr.*, **201**, 263 (1992).
9. I. Vencato, E. Mattievich, and Y. P. Mascarenhas, "Crystal structure of synthetic lipscombite: a redetermination," *Am. Mineral.*, **74**(3-4), 456 (1989).
10. I. Vencato, E. Mattievich, and Y. P. Mascarenhas, "Crystal structure of synthetic lipscombite: a redetermination," *Acta Cryst. A*, **43**, C153 (1987).
11. M. L. Lindberg and C. L. Christ, "Crystal structures of the isostructural minerals lazulite, scorzalite and barbosalite," *Acta Cryst.*, **12**, 695 (1959).
12. M. Dollé, S. Patoux, and T. J. Richardson, "Lithium insertion chemistry of phosphate phases with the lipscombite structure," *J. Power Sources*, **144**(1), 208 (2005).
13. Z. Wang, S. Sun, F. Li, G. Chen, D. Xia, T. Zhao, W. Chu, and Z. Wu, "Stability, electrochemical behaviors and electronic structures of iron hydroxyl-phosphate," *Mater. Chem. Phys.*, **123**(1), 28 (2010).
14. S. Sun, Z. Wang, and D. Xia, "Theoretical study of a new cathode material of Li-battery: Iron hydroxyl-phosphate," *J. Phys. Chem. C*, **114**(1), 587 (2010).
15. S. M. Zhang, J. X. Zhang, S. J. Xu, X. J. Yuan, and T. Tan, "Synthesis, morphological analysis and electrochemical performance of iron hydroxyl phosphate as a cathode material for lithium ion batteries," *J. Power Sources*, **243**, 274 (2013).
16. S. Han, J. Wang, S. Li, D. Wu, and X. Feng, "Graphene aerogel supported Fe$_5$(PO$_4$)$_4$(OH)$_3$·2H$_2$O microspheres as high performance cathode for lithium ion batteries," *J. Mater. Chem. A*, **2**, 6174 (2014).
17. Y. D. Yu, Y. J. Zhu, and J. Wu, Glycerin-assisted solvothermal synthesis of Fe$_3$(PO$_4$)$_2$(OH)$_2$ microspheres, *Materials Letters*, **205**, 158 (2017).
18. C. Karegeya, A. Mahmoud, R. Cloots, B. Vertruyen, and F. Boschini, "Hydrothermal synthesis in presence of carbon black: Particle-size reduction of iron hydroxyl phosphate hydrate for Li-ion battery," *Electrochim. Acta*, **250**, 49 (2017).
19. A. Mahmoud, C. Karegeya, M. T. Sougrati, J. Bodart, B. Vertruyen, R. Cloots, P. E. Lippens, and F. Boschini, "Electrochemical Mechanism and Effect of Carbon Nanotubes on the Electrochemical Performance of Fe$_{1.19}$(PO$_4$)(OH)$_{0.57}$(H$_2$O)$_{0.43}$ Cathode Material for Li-Ion Batteries," *ACS Appl. Mater. Interfaces*, **10**(40), 34202 (2018).
20. C. Henriksen, C. Wegeberg, and D. B. Ravnsbæk, "Phase Transformation Mechanism of Li-Ion Storage in Iron(III) Hydroxide Phosphates," *J. Phys. Chem. C*, **122**(4), 1930 (2018).
21. B. L. Ellis and L. F. Nazar, "Anion-induced solid solution electrochemical behavior in iron tavorite phosphates," *Chem. Mater.*, **24**(6), 966 (2012).
22. G. Zhou, X. Duan, B. Liu, Q. Li, and T. Wang, "Architectures of tavorite LiFe(PO$_4$)(OH)$_{0.5}$F$_{0.5}$ hierarchical microspheres and their lithium storage properties," *Nanoscale*, **6**(19), 11041 (2014).
23. H. Yaghoobnejad Asl and A. Choudhury, "Phosphorous acid route synthesis of iron tavorite phases, LiFePO$_4$(OH)$_x$F$_{1-x}$ [0 ≤ x ≤ 1] and comparative study of their electrochemical activities," *RSC Adv.*, **4**(71), 37691 (2014).
24. M.-Y. Cho, Y. S. Lim, S.–M. Park, K.–B. Kim, and K. C. Roh, "Size-tunable tavorite LiFe(PO4)(OH) microspheres with a core-shell structure," *CrystEngComm*, **17**(32), 6149 (2015).
25. J. M. M. Millet and D. Rouzies, "Mössbauer spectroscopic study of synthetic lipscombite and barbosalite at room temperature," *Hyperfine Interact.*, **77**, 11 (1993).
26. Bruker-SMART. Bruker AXS Inc., Madison, Wisconsin, USA. 2002.
27. Bruker- SAINT, SADABS and SHELXTL. Bruker AXS Inc., Madison, Wisconsin, USA, 2008.
28. G. M. Sheldrick, "A short history of SHELX," *Acta Cryst.*, **A64**, 112 (2008).
29. A. L. Spek, "Structure validation in chemical crystallography," *Acta Cryst.*,**65D**, 148 (2009).
30. G. M. Sheldrick, C. B. Hubshle, and B. Dittrich, "Shelxle: A Qt graphical user interface for SHELXL," *J. Appl. Cryst.*, **44**, 1281 (2011).
31. B. H. Toby and R. B. Von Dreele, "GSAS-II: the genesis of a modern open-source all-purpose crystallography software package," *J. Appl. Cryst.*, **46**, 544 (2013).
32. K. Lagarec and D. G. Rancourt, "Extended Voigt-based analytic lineshape method for determining N-dimensional correlated hyperfine parameter distributions in Mössbauer spectroscopy." *Nucl. Instrum. Methods Phys. Res., Sect. B*, **129**, 266 (1997).
33. P. Sandineni, H. Yaghoobnejad Asl, and A. Choudhury, "Kagomé lattices as cathode: Effect of particle size and fluoride substitution on electrochemical lithium insertion in sodium- and ammonium-Jarosites," *J. Solid State Chem.*, **242**, 78 (2016).
34. G. J. Redhammer, G. Tippelt, G. Roth, W. Lottermoser, and G. Amthauer, "Structure and Mössbauer spectroscopy of barbosalite Fe^{2+}Fe$_2^{3+}$(PO$_4$)(OH) between 80 K and 300 K," *Phys. Chem. Miner.*, **27**(6), 419 (2000).
35. F. Menil, "Systematic trends of the ^{57}Fe Mössbauer isomer shifts in (FeO$_n$) and (FeF$_n$) polyhedra. Evidence of a new correlation between the isomer shift and the inductive effect of the competing bond T −X (→ Fe) (where X is O or F and T any element with a formal positive charge)." *J. Phys. Chem. Solids*, **46**, 763 (1985).
36. M. C. Smart, B. V. Ratnakumar, and S. Surampudi, "Electrolytes for Low-Temperature Lithium Batteries Based on Ternary Mixtures of Aliphatic Carbonates," *J. Electrochem. Soc.*, **146**, 486 (1999).
37. T. R. Jow, S. A. Delp, J. L. Allen, J.–P. Jones, and M. C. Smart, "Factors limiting Li$^+$ charge transfer kinetics in Li-ion batteries," *J. Electrochem. Soc.*, **165**, A361 (2018).
38. W. Yang, Y. Bi, Qin Y, Y. Liu, X. Zhang, B. Yang, Q. Wu, D. Wang, and S. Shi, "LiMn$_{0.8}$Fe$_{0.2}$PO4/C cathode material synthesized via co-precipitation method with superior high-rate and low-temperature performances for lithium-ion batteries," *J. Power Sources*, **275** (2015).
39. M. Satyanarayana, R. S. Rao, V. Pralong, and U. V. Varadaraju, "Reversible Li Insertion Studies on V$_4$O$_3$(PO$_4$)$_3$ as High Energy Storage Material for Li-Ion Battery Applications," *J. Electrochem. Soc.*, **164**, A6201 (2017).